A High-Order AMR Algorithm for Chemically Reacting Flows

Cosmin Safta, Jaideep Ray, Habib N. Najm
Sandia National Laboratories
Livermore, USA

1 Introduction

Chemical reacting systems based on hydrocarbon fuels typically exhibit a large spectrum of characteristic spatial and temporal scales. The complexity of kinetic models even for simple hydrocarbon fuels compounds this problem making multidimensional numerical simulations difficult even for laboratory scale configurations.

These difficulties are commonly addressed in a variety of ways. For low speed flows, one may assume that acoustic waves travel at infinite speed and adopt a low Mach number approximation of the Navier-Stokes equations [1]. The structure of the governing equations can also be exploited for an operator-split construction, performing the transport and reactive time-advancement via specialized integrators [2]. In problems where fine structures exist only in a small fraction of the domain e.g. in laminar jet flames, one may employ adaptive mesh refinement (AMR) [3] to concentrate resolution only where needed [4–7], while maintaining a coarse mesh resolution elsewhere.

We have recently developed a numerical model that aims to address some of the challenges posed by the use of AMR for reacting flow computations. In order to reduce the number of grid points and the number of refinement levels in the computational mesh hierarchy, we employ high-order stencils to discretize the transport equations and to interpolate between the computational blocks on adjacent mesh levels. Further, we employ a projection scheme for the momentum transport on a *uniform* mesh, that is coupled with the adaptive mesh solution of the scalar transport equations. This hybrid construction is driven by a number of practical considerations, as further detailed in the next section. For ease of implementation with AMR, we employ an extended-stability Runge Kutta Chebyshev (RKC) scheme [8] to time-advance the system. The 2D numerical scheme developed in this investigation is designed to work with block-structured adaptively refined meshes (alternatively, structured adaptive mesh refinement, SAMR).

2 Numerical Approach

In this section we describe the numerical construction used to solve the low Mach number reacting flow equations. In the low-Mach number limit, the continuity, momentum and scalar equations are written in

Correspondence to: csafta@sandia.gov

compact form as

$$\nabla \cdot \mathbf{v} = -\frac{1}{\rho}\frac{D\rho}{Dt} \tag{1a}$$

$$\frac{\partial \mathbf{v}}{\partial t} = -\frac{1}{\rho}\nabla p + C_U + D_U \tag{1b}$$

$$\frac{\partial T}{\partial t} = C_T + D_T + S_T \tag{1c}$$

$$\frac{\partial Y_k}{\partial t} = C_{Y_k} + D_{Y_k} + S_{Y_k} \qquad k = 1, 2, \ldots, N_s \tag{1d}$$

Here $\mathbf{v}$ is the velocity vector, ρ the density, T the temperature, Y_k the mass fraction of species k, p is the hydrodynamic pressure, and N_s is the number of chemical species. The D/Dt operator in the continuity equation represents the material derivative. The system of governing equations is closed with the equation of state for an ideal gas:

$$P_0 = \frac{\rho \Re T}{\overline{W}} = \rho \Re T \sum_{k=1}^{N_s} \frac{Y_k}{W_k} = \text{const} \rightarrow \frac{1}{\rho}\frac{D\rho}{Dt} = -\frac{1}{T}\frac{DT}{Dt} - \sum_{k=1}^{N_s} \frac{\overline{W}}{W_k}\frac{DY_k}{Dt} \tag{2}$$

where P_0 is the thermodynamic pressure, $\Re$ is the universal gas constant, W_k is the molecular weight of species k, and $\overline{W}$ is the molecular weight of the mixture. The thermodynamic pressure is spatially uniform in the low-Mach number limit. Further, restricting our focus to flows in open domains, P_0 is constant. A detailed description of the convection C_*, diffusion D_*, and source terms S_* in the *rhs* of equations (1a-1d) is given in [9].

The divergence constraint (eq. 1a) resulting from the low Mach number limit leads to a differential algebraic equation system, for which we adopt a projection method to solve for the velocity and pressure fields. The momentum solver is coupled with a solver for the species and temperature fields, arriving at an overall construction that is fourth-order in space, second-order in time.

As described in Section 1, the problem is solved on a mesh hierarchy. On a given patch, variables are defined at cell centers and edge-centers. The temperature, density, pressure, and species mass fractions are located at cell centers, while the velocity components are located at edge centers.

The numerical integration of the system of equations is performed in three stages. First, a projection approach is adopted to advance the velocity field based on the equations (1a-1b). The projection scheme is implemented on a uniform mesh. In the second stage, the scalars are advanced using an operator split approach that separates the convection and diffusion contributions from the ones due to the chemical source terms. We implement a symmetric Strang splitting scheme beginning with the source term contribution for half the time step, followed by the contributions from convection and diffusion terms for a full time step, and concluded by the remaining contribution from the reaction term for half the time step. During this stage, scalars are recursively advanced on successively refined grids necessary to resolve the scalar spatial structures. The time stepping is concluded with the third stage, which repeats the projection algorithm on a uniform mesh using information on scalar fields obtained at the end of the second step. The algorithm is described in detail below.

Stage 1_a

A 2$^{\text{nd}}$order Adams-Bashforth scheme is used to advance the velocity field using momentum and diffusion terms only

$$\frac{\hat{\mathbf{v}}^{n+1} - \mathbf{v}^n}{\Delta t} = \left(1 + \frac{1}{2}\frac{\Delta t}{\Delta t_o}\right)\left(C_U^n + D_U^n\right) - \frac{1}{2}\frac{\Delta t}{\Delta t_o}\left(C_U^{n-1} + D_U^{n-1}\right) \tag{3}$$

Superscripts n and $n-1$ refer to values at the current t^n and previous t^{n-1} times, respectively. The above expression takes into account changes in time step values, $\Delta t = t^{n+1} - t^n$ and $\Delta t_o = t^n - t^{n-1}$.

The convection terms contain components that are either collocated or staggered. Derivatives are discretized using 4$^{\text{th}}$ order stencils. Interpolations between cell-centers and edge-centers are 6$^{\text{th}}$ order accurate in order to preserve the overall 4$^{\text{th}}$ order accuracy of the scheme. The stencils for the these discretizations are given elsewhere [9, 10].

Stage 1_b
The provisional velocity field, $\hat{\mathbf{v}}$, does not satisfy eq. (1a). This equation is used in conjunction with eq. (1b) to derive an equation for the hydrodynamic pressure field

$$\nabla \cdot \left(\frac{1}{\rho^{n+1}} \nabla p \right) = \frac{1}{\Delta t} \left(\nabla \cdot \hat{\mathbf{v}}^{n+1} + \frac{1}{\rho} \frac{D\rho}{Dt} \bigg|^{n+1} \right), \tag{4}$$

that will be then used to correct the provisional velocity field. Since the scalar fields at t^{n+1} are not yet known, $\frac{1}{\rho}\frac{D\rho}{Dt}\Big|^{n+1}$ is estimated by extrapolation using its values at t^n and t^{n-1}. The numerical evaluation at previous time steps of $\frac{1}{\rho}\frac{D\rho}{Dt}$ is described in Stage 3_b. The density at t^{n+1}, ρ^{n+1}, is also extrapolated from values at t^n and t^{n-1}. The projection scheme for the momentum solution adapts a finite-volume construction from [11] to finite differences, in order to achieve a consistent 4$^{\text{th}}$ order construction for the pressure (Poisson) solve. The variable coefficient Poisson problem is solved using a conjugate-gradient method, preconditioned with a multigrid technique in the *hypre* package [12] to accelerate the convergence rate.

Stage 1_c
The gradient of the hydrodynamic pressure is used to correct the provisional velocity field $\hat{\mathbf{v}}^{n+1}$ to obtain the predicted velocity at $n+1$

$$\mathbf{v}^{n+1,p} = \hat{\mathbf{v}}^{n+1} - \frac{\Delta t}{\rho^{n+1}} \nabla p, \tag{5}$$

Superscript p was added to $\mathbf{v}$ to distinguish the predicted velocity values obtained at the end of Stage 1 from the corrected ones obtained at the end of Stage 3 below.

Stage 2_a
In the first part of the second stage, temperature and species mass fractions are advanced over half the time step based on contributions from the source terms, S_T and S_{Y_k}.

$$\begin{aligned} T^* - T^n &= \int_{\Delta t/2} S_T dt \\ Y_k^* - Y_k^n &= \int_{\Delta t/2} S_{Y_k} dt \qquad k = 1, 2, \ldots, N_s \end{aligned} \tag{6}$$

The CVODE stiff integrator package [13] is used to integrate eqs. (6). At the end of the stage, the scalar values are recursively restricted from fine to coarse grid levels. Stencils for interpolations between coarse and fine grid levels are 6$^{\text{th}}$-order.

Stage 2_b
During the second part of the second stage, a 2$^{\text{nd}}$-order, multi-stage, Runge-Kutta-Chebushev (RKC) [8]

scheme is used to advance scalars based on the contributions from convection and diffusion terms:

$$\begin{aligned} T^{**} - T^{*} &= \int_{t^n}^{t^{n+1}} \underbrace{C_T + D_T}_{F_T} dt \\ Y_k^{**} - Y_k^{*} &= \int_{t^n}^{t^{n+1}} \underbrace{C_{Y_k} + D_{Y_k}}_{F_{Y_k}} dt \qquad k = 1, 2, \ldots, N_s \end{aligned} \tag{7}$$

The numerical details for the multi-stage RKC scheme are given elsewhere [2, 8].

As scalars are advanced from t^n to t^{n+1}, velocity values needed to construct advection fluxes for the intermediate RKC times are computed by interpolation based on the values at t^n and $\mathbf{v}^{n+1,p}$ at $t^{n+1} = t^n + \Delta t$. Similar to some of the velocity convection terms, scalar convection and diffusion terms involve components that are not collocated. For these terms scalar derivatives are evaluated using 4^{th} order staggered derivative stencils, while interpolations use 6^{th} order stencils. This results in the computation of convective and diffusive terms at cell centers. They are then used to advance the scalar values with the RKC algorithm, applied recursively using the Berger-Collela time refinement [3] on successively refined mesh levels.

Stage 2_c
Stage 2_c is a repeat of Stage 2_a, using the "**" scalar values as initial conditions. At the end of this stage all scalars correspond to t^{n+1} and the solution needs to be restricted (fine-to-coarse grid interpolation) recursively starting from the finest grid level in the main hierarchy.

Stage 3_a
The provisional velocity field values at t^{n+1} are re-evaluated based on the scalar values obtained at the end of Stage 2 and on the predicted velocity values at the end of Stage 1

$$\frac{\hat{\mathbf{v}}^{n+1} - \mathbf{v}^n}{\Delta t} = \frac{1}{2}\left((C_U^n + D_U^n) + \left(C_U^{n+1} + D_U^{n+1}\right)\right) \tag{8}$$

The convection C_U^{n+1} and diffusion D_U^{n+1} are based on the velocity field $\mathbf{v}^{n+1,p}$ and the scalar values at t^{n+1}.

Stage 3_b
The hydrodynamic pressure field is re-computed using equation (4). The divergence term that enters the right hand side of this equation is constructed using the provisional velocity field obtained in Stage 3_a, while eq. (2) is used to compute $\frac{1}{\rho}\frac{D\rho}{Dt}\Big|^{n+1}$ based on scalar values at t^{n+1}, obtained in Stage 2.

Stage 3_c
This stage is similar to Stage 1_c. The gradient of the hydrodynamic pressure obtained at Stage 3_b is used to correct $\hat{\mathbf{v}}^{n+1}$ (computed at Stage 3_a) to obtain $\mathbf{v}^{n+1}$.

3 Results

Results for 2D vortex pair - flame interactions are used to verify the stability and accuracy of the numerical construction. All reacting flow tests involve methane combustion. Flame results for GRI-Mech 3.0 (53 species, 325 elementary reactions) [14] are shown to highlight the benefits of this numerical approach in capturing the inner flame structure efficiently. Due to the computational expense, the convergence rate is measured in simulations with chemistry modeled using a C1 skeletal mechanisms (16 species, 46 reversible reactions).

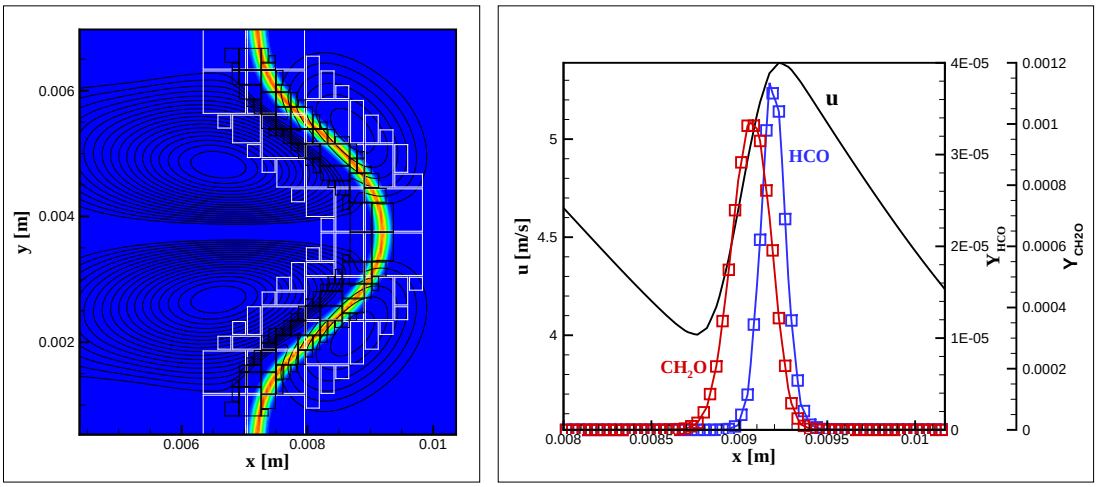

Figure 1: Left frame: Vorticity contours (black lines) and HCO mass fraction (colormap) during the interaction between a vortex pair and an initially flat premixed flame. The vorticity contours are shown on level 0, while the mass fraction colormap is shown on levels 1 and 2. Right frame: streamwise velocity u and and species mass fraction profiles along a centerline slice.

Δx range [μm]	T	ρ	u	v	∇p_x	∇p_y	Y_{CH_4}	Y_{O_2}	Y_{CO_2}	Y_{CH_3}	Y_{HCO}
$15 \rightarrow 30 \rightarrow 60$	3.9	4.0	3.8	3.7	3.8	3.7	3.9	3.9	3.9	3.9	4.1

Table 1: Spatial convergence rates for $2D$ vortex-pair flame interactions using 2 level mesh and a C1-mechanism. Solutions are advanced with a time step $\Delta t = 2 \times 10^{-8}$ s and errors are measured after $t = 0.3$ ms from the beginning of the simulations.

Figure 1 shows a snapshot of the vorticity and HCO mass fraction fields (left frame) and velocity and species mass fraction profiles along a centerline slice through the flame (right frame) at $t = 0.4$ ms from the beginning of the simulation. At this time the flame, simulated with GRI-Mech 3.0, is contorted by the vortex pair and the centerline region is significantly compressed by the velocity field induced by the vortex. The species mass fraction profiles in the right frame show that radical profiles are thinner than the velocity field length scales in the flame region. This indicates that mesh refinement is only necessary for resolving inner flame structure, while the spatial length scales associated with the flow can be captured on the lowest level of the SAMR hierarchy only.

The results in Table 1 show the spatial convergence rates for the 2D flame-vortex configuration obtained with the 16 species C1 kinetic model. Roughly 4^{th}-order convergence rate is observed for all variables.

4 Conclusions

This paper describes a high-order numerical model for the simulation of chemically reacting flow in the low-Mach number limit. A 4^{th} order (in space) projection algorithm for the momentum transport is coupled to a 4^{th} order-in-space, 2^{nd} order-in-time scheme for the solution of the equations of transport of energy and species mass fractions on a block-structured adaptively refined mesh. Finite differences are used to approximate spatial derivatives.

The primary reason for constructing a 4^{th}-order adaptive mesh refinement scheme was to reduce the number of cells in the entire problem, prior to using it with detailed (and stiff) kinetic mechanisms

in reacting flow studies. Chemistry integration costs are expected to dominate and efficiency/usability gains are tied to using shallow grid hierarchies and to keeping the number of cells at a "manageable" level, while resolving the flame structure adequately. Future efforts will be devoted to such problems and will necessarily exploit massive parallelism in computations.

References

[1] A. Majda and J. Sethian, "The derivation and numerical solution of the equations for zero mach number combustion," *Comb. Sci. and Technology*, vol. 42, pp. 185–205, 1985.

[2] H. Najm and O. Knio, "Modeling Low Mach Number Reacting Flow with Detailed Chemistry and Transport," *J. Sci. Comp.*, vol. 25, no. 1, pp. 263–287, 2005.

[3] M. Berger and P. Colella, "Local adaptive mesh refinement for shock hydrodynamics," *J. Comput. Phys.*, vol. 82, pp. 64–84, 1989.

[4] B. Bennett and M. Smooke, "Local rectangular refinement with application to axisymmetric laminar flames," *Combust. Theor. Model.*, vol. 2, pp. 221–258, SEP 1998.

[5] J. Ray, H. Najm, R. Milne, K. Devine, and S. Kempa, "Triple flame structure and dynamics at the stabilization point of an unsteady lifted jet diffusion flame," *Proc. Combust. Inst.*, vol. 28, pp. 219–226, 2000. Part 1.

[6] M. Day and J. Bell, "Numerical simulation of laminar reacting flows with complex chemistry," *Combust. Theor. Model.*, vol. 4, pp. 535–556, DEC 2000.

[7] M. Anthonissen, B. Bennett, and M. Smooke, "An adaptive multilevel local defect correction technique with application to combustion," *Combust. Theor. Model.*, vol. 9, pp. 273–299, MAY 2005.

[8] J. G. Verwer, B. Sommeijer, and W. Hundsdorfer, "RKC Time-Stepping for Advection-Diffusion-Reaction Problems," *J. Comput. Phys.*, vol. 201, no. 1, pp. 61–79, 2004.

[9] C. Safta, J. Ray, and H. Najm, " A High-Order Low-Mach Number AMR Construction for Chemically Reacting Flows," *J. Comput. Phys.*, vol. 229, no. 24, pp. 9299–9322, 2010.

[10] J. Ray, C. Kennedy, S. Lefantzi, and H. Najm, "Using High-Order Methods on Adaptively Refined Block-Structured Meshes," *SIAM J. Sci. Comp.*, vol. 29, no. 1, pp. 139–181, 2007.

[11] S. Kadioglu, R. Klein, and M. Minion, "A fourth-order auxiliary variable projection method for zero-Mach number gas dynamics," *J. Comput. Phys.*, vol. 227, pp. 2012–2043, 2008.

[12] "hypre: High performance preconditioners." `http://computation.llnl.gov/casc/hypre`.

[13] S. D. Cohen and A. C. Hindmarsh, "CVODE, a Stiff/Nonstiff ODE Solver in C," *Comput. Phys.*, vol. 10, no. 2, pp. 138–143, 1996.

[14] G. Smith, D. Golden, M. Frenklach, N. Moriarty, B. Eiteneer, M. Goldenberg, C. Bowman, R. Hanson, S. Song, W. G. Jr., V. Lissianski, and Q. Zhiwei *www.me.berkeley.edu/gri_mech/*.